

# Quantifying modelling uncertainties when combining multiple gravitational-wave detections from binary neutron star sources

Nina Kunert<sup>1</sup>, Peter T. H. Pang<sup>2,3</sup>, Ingo Tews<sup>4</sup>, Michael W. Coughlin<sup>5</sup>, and Tim Dietrich<sup>1,6</sup>

<sup>1</sup>*Institute for Physics and Astronomy, University of Potsdam, D-14476 Potsdam, Germany*

<sup>2</sup>*Nikhef, Science Park 105, 1098 XG Amsterdam, The Netherlands*

<sup>3</sup>*Institute for Gravitational and Subatomic Physics (GRASP),*

*Utrecht University, Princetonplein 1, 3584 CC Utrecht, The Netherlands*

<sup>4</sup>*Theoretical Division, Los Alamos National Laboratory, Los Alamos, NM 87545, USA*

<sup>5</sup>*School of Physics and Astronomy, University of Minnesota, Minneapolis, Minnesota 55455, USA and*

<sup>6</sup>*Max Planck Institute for Gravitational Physics (Albert Einstein Institute), Am Mühlenberg 1, Potsdam 14476, Germany*

(Dated: October 25, 2021)

With the increasing sensitivity of gravitational-wave detectors, we expect to observe multiple binary neutron-star systems through gravitational waves in the near future. The combined analysis of these gravitational-wave signals offers the possibility to constrain the neutron-star radius and the equation of state of dense nuclear matter with unprecedented accuracy. However, it is crucial to ensure that uncertainties inherent in the gravitational-wave models will not lead to systematic biases when information from multiple detections are combined. To quantify waveform systematics, we perform an extensive simulation campaign of binary neutron-star sources and analyse them with a set of four different waveform models. Based on our analysis with about 38 simulations, we find that statistical uncertainties in the neutron-star radius decrease to  $\pm 250\text{m}$  (2% at 90% credible interval) but that systematic differences between currently employed waveform models can be twice as large. Hence, it will be essential to ensure that systematic biases will not become dominant in inferences of the neutron-star equation of state when capitalizing on future developments.

## I. INTRODUCTION

Gravitational waves (GWs) emitted from binary neutron-star (BNS) coalescences allow us to probe the equation of state (EOS) of dense nuclear matter. This was successfully demonstrated by the LIGO-Virgo Collaboration and other research groups following the first GW observation of a BNS system, GW170817, using Bayesian analyses of the GW signal [1–5]. Such constraints have been further improved in numerous multi-messenger analyses, e.g., Refs. [3, 6–16], by incorporating data from associated electromagnetic observations, AT2017gfo and GRB170817A [17], nuclear-physics computations [7, 18, 19], nuclear-physics experiments [20–22], as well as radio and X-ray observations of isolated neutron stars (NSs) [23–29].

Extracting information from observational data always requires certain modeling assumptions. For example, to infer information from the measured GW data it is necessary to cross-correlate the observed GW signal with theoretical models describing the compact binary coalescence for various binary parameters. Following this approach, the matching introduces systematic uncertainties that originate from the approximations made to describe the general relativistic two-body problem. These approximations range from an analytical description using the Post-Newtonian (PN) framework [30], the effective-one-body (EOB) model [31, 32] to numerical-relativity simulations, e.g., Refs. [33, 34]. Since it is expected that statistical uncertainties will be reduced for high signal-to-noise ratio (SNR) signals or when multiple signals are combined, systematic uncertainties introduced by the waveform models will become increasingly prominent and it is crucial

to understand all sources of systematic uncertainties for a reliably quantification of EOS constraints.

Previous studies have shown that EOS constraints based on tidal deformabilities extracted from GW170817 were dominated by statistical uncertainties, e.g., Ref. [3], and that systematic biases were under control, i.e., noticeably smaller than statistical ones. For example, Ref. [35] used an injection study to investigate systematic uncertainties by using different gravitational waveform models in the parameter estimation for GW170817. The authors concluded that for GW170817 no systematic bias is expected but that for GW170817-like sources observed with Advanced LIGO and Advanced Virgo design sensitivity different waveform models can lead to noticeable biases, i.e., the recovered 90% credible intervals would not contain the injected values. Similarly, Ref. [36] used simulated, non-spinning GW170817-like BNS sources measured at design sensitivity and found that for unequal mass systems the obtained tidal parameters can get noticeably biased. Ref. [37] extended this work by studying the imprint of precession as well as the source localization obtained through a possible electromagnetic counterpart. Ref. [38] introduced a method to quantify systematic biases during parameter estimation and found that existing GW waveform models used for the analysis of GW170817 will be dominated by systematic uncertainties for SNRs above 80. Finally, very recently, Ref. [39] also discussed numerous systematic biases that enter GW analyses and quantified the waveform accuracy required to achieve the radius measurement projected for Voyager and 3G detectors, outlining the importance of waveform systematics.

As pointed out in, e.g., Refs. [40–43], even low SNR

signals can be used and combined to constrain the tidal deformability parameter to an accuracy of  $\sim 10\%$  with only a few tens of detections; cf. also Refs. [44, 45]. Using such a procedure, systematic biases are introduced through “stacking,” i.e., combining multiple GW measurements. However, to our knowledge no study has addressed waveform systematics introduced through the stacking of signals within a realistic injection study employing state-of-the-art waveform models. Here, we address this issue to determine at which point systematic biases dominate. We use a set of 40 simulated signals analysed with four different waveform models and perform a total of 160 BNS parameter estimation simulations assuming Advanced GW detectors at design sensitivity [46, 47] to estimate systematic biases.<sup>1</sup>

The article is structured as follows: In Sec. II, we describe numerical methods, employed waveform models, and our injection setup. In Sec. III, we discuss our results and summarize and conclude our main findings in Sec. IV. Throughout this work, geometric units are used by setting  $G = c = 1$ . Further notations are  $M = M_A + M_B$  for a system’s total mass,  $q = M_A/M_B$  for the mass ratio, and  $\Lambda_A, \Lambda_B$  for individual tidal deformabilities of the stars.

## II. METHODS

### A. Bayesian Inference

By using Bayes’ theorem, the posterior  $p(\vec{\theta}|d, \mathcal{H})$  on the parameters  $\vec{\theta}$  under hypothesis  $\mathcal{H}$  and with data  $d$  is given by

$$p(\vec{\theta}|d, \mathcal{H}) = \frac{p(d|\vec{\theta}, \mathcal{H})p(\vec{\theta}|\mathcal{H})}{p(d|\mathcal{H})}, \quad (1)$$

where  $p(d|\vec{\theta}, \mathcal{H})$ ,  $p(\vec{\theta}|\mathcal{H})$ , and  $p(d|\mathcal{H})$  are the likelihood, prior, and evidence, respectively. The prior describes our knowledge of the parameters before the observation. It also naturally acts as a gateway for additional observations to be included as part of the analysis. The likelihood quantifies how well the hypothesis describes the data at a given point  $\theta$  in the parameter space and the evidence marginalizes over the whole parameter space. By assuming Gaussian noise, the likelihood  $p(d|\vec{\theta}, \mathcal{H})$  of a GW signal  $h(\vec{\theta})$  with parameters  $\vec{\theta}$  embedded in the data  $d$  is given by [48]

$$p(d|\vec{\theta}, \mathcal{H}) \propto \exp\left(-2 \int_{f_{\text{low}}}^{f_{\text{high}}} \frac{|\tilde{d}(f) - \tilde{h}(f; \vec{\theta})|^2}{S_n(f)} df\right), \quad (2)$$

where  $\tilde{n}(f)$  and  $\tilde{h}(f)$  are the Fourier transform of  $n(t)$  and  $h(t; \vec{\theta})$ ,  $S_n(f)$  is the one-sided power spectral density of the noise. In our study, all simulations are performed in Gaussian noise assuming Advanced LIGO [46] and Advanced Virgo [47] design sensitivity and we set  $f_{\text{low}}$  and  $f_{\text{high}}$  to 20 Hz and 2048 Hz.

The evidence  $p(d|\mathcal{H})$  is given by

$$p(d|\mathcal{H}) = \int_{\mathcal{V}} p(d|\vec{\theta}, \mathcal{H})p(\vec{\theta}|\mathcal{H})d\vec{\theta}, \quad (3)$$

which is the normalization constant for the posterior distribution. The landscape of the likelihood function is explored using the nested sampling algorithm [49] implemented in PARALLEL BILBY [50].

### B. Combining information from multiple detections

Extracting tidal effects from GW data requires information about the EOS. In this study, we will use EOSs that are constrained by chiral effective field theory (EFT) at low densities [19, 51]. Chiral EFT is a systematic theory for nuclear forces that provides an order-by-order scheme for the interactions among neutrons and protons [52, 53]. These interactions can then be used in microscopic studies of dense matter up to densities of  $\sim 2$  times the nuclear saturation density ( $n_{\text{sat}} = 0.16 \text{ fm}^{-3}$ ). In Ref. [13], 5000 EOSs constrained by quantum Monte Carlo calculations using chiral EFT interactions up to  $1.5n_{\text{sat}}$  were computed. For this article, we employ the most-likely EOS of Ref. [13] for our injections. With regard to the recovery, we are using the same set of 5000 EOSs, but taking into account the mass measurements of PSR J0348+4042[23], PSR J1614-2230[54], and PSR J0740+6620[55] in the prior, similar to the approach taken in Ref [13]. In contrast to Ref [13], the NICER observation on PSR J0030+0451[26, 27] and the upper bound of maximum mass derived from GW170817[56] are not included. As including additional experiments can potentially mask the systematics induced in GW analysis.

To sample over the EOS, we add a “hyperparameter”. Hence, we compute the tidal deformability distribution for a given mass and EOS via

$$p(\Lambda_i|m_i, \text{EOS}) = \delta(\Lambda_i - \Lambda(m_i; \text{EOS})), \quad (4)$$

with  $m_i$  and  $\Lambda_i$  denoting the mass and tidal deformability of the stars. In addition to the tidal behavior, the EOS also determines the maximum allowed mass  $M_{\text{max}}$  for NSs. Therefore, we choose a uniform NS mass distribution given by

$$p(m_1, m_2|\text{EOS}) = \frac{2\Theta(m_1 - m_2)\Theta(M_{\text{max}} - m_1)}{(M_{\text{max}} - M_{\text{min}})^2}, \quad (5)$$

where  $M_{\text{min}}$  is the minimum NS mass and  $\Theta$  is the Heaviside step function. We choose  $M_{\text{min}}$  to be  $0.5M_{\odot}$ .

<sup>1</sup> We note that two simulated BNS sources did not converge in the parameter estimation. Therefore, our analysis will be based on the remaining 38 simulations.

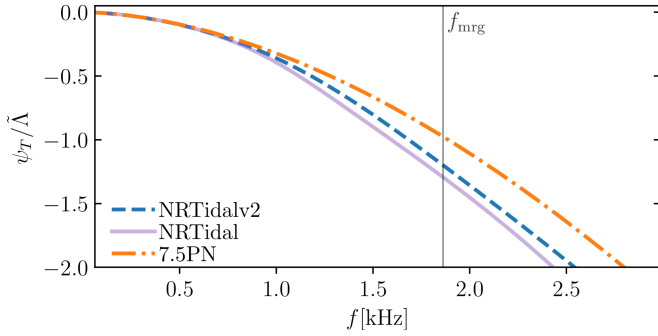


FIG. 1. Frequency dependence of the tidal phase within the 7.5PN order (orange), NRTidal (purple), and NRTidalv2 (blue) model. For comparison, we show the merger frequency for an irrotational, equal-mass binary with  $M_1 = M_2 = 1.35M_\odot$  and  $\tilde{\Lambda} = 392$ , cf. Ref. [59].

The joint posterior for the EOS with  $N_{\text{obs}}$  detections  $\{d_i\}$  is then given by [57]

$$p(\{\vec{d}_i\}|\text{EOS}) = \prod_{i=1}^{N_{\text{obs}}} \frac{\int d\vec{\theta} p(\vec{d}_i|\vec{\theta}) p(\vec{\theta}|\text{EOS})}{\int d\vec{\theta} p_{\text{det}}(\vec{\theta}) p(\vec{\theta}|\text{EOS})}, \quad (6)$$

where  $p_{\text{det}}(\vec{\theta})$  is the probability of detecting the GW signal corresponding to the source parameters  $\vec{\theta}$ . In this work, a threshold SNR of 7 is enforced for the detections and we estimate  $p_{\text{det}}(\vec{\theta})$  using a neural-network classifier as described in Ref. [58].

### C. Waveform Models

The frequency-domain representation of a gravitational waveform can be written as

$$\tilde{h}(f) = \tilde{A}(f) e^{-i\psi(f)}, \quad (7)$$

with the frequency  $f$ , the amplitude  $\tilde{A}(f)$ , and GW phase  $\psi(f)$ . The phase can be further decomposed into

$$\psi(f) = \psi_{\text{pp}}(f) + \psi_{\text{SO}}(f) + \psi_{\text{SS}}(f) + \psi_{\text{T}}(f) + \dots, \quad (8)$$

with  $\psi_{\text{pp}}$  being the non-spinning point-particle contribution,  $\psi_{\text{SO}}$  corresponding to contributions caused by spin-orbit coupling,  $\psi_{\text{SS}}$  to contributions caused by spin-spin effects, and  $\psi_{\text{T}}$  denoting the tidal effects present in the GW phase. We note that higher-order effects, e.g., cubic-in-spin, could also be included.

The dominant quantity describing EOS-related tidal effects on the GW signal is the mass-weighted tidal deformability [44, 60, 61]

$$\tilde{\Lambda} = \frac{32}{39} \left[ \left( 1 + 12 \frac{X_B}{X_A} \right) \left( \frac{X_A}{C_A} \right)^5 k_2^A + (A \leftrightarrow B) \right], \quad (9)$$

with the compactness parameters of the individual undisturbed stars  $C_{A,B} = M_{A,B}/R_{A,B}$ , the Love numbers

$k_2^{A,B}$  [61–63], and  $X_{A,B} = M_{A,B}/(M_A + M_B)$ . The leading-order PN contribution to the tidal phase, which is proportional to  $\tilde{\Lambda}$ , starts at the 5PN order, i.e., becomes most relevant at the late inspiral; cf. Fig. 2 of Ref. [34]. To quantify the modelling systematics, we employ four different GW waveform models. These are based on different point-particle and tidal descriptions and, hence, lead to different estimates on the extrinsic source properties. The models and their main properties are described below.

*TaylorF2 (TF2)* is a purely analytical model derived within the Post-Newtonian approximation, see Ref. [30] for a review. The model includes point-particle [64–69] and aligned spin terms [69–72] up to 3.5PN order as well as tidal effects up to 7.5PN order [73–76].<sup>2</sup>

*IMRPhenomD-NRTidal (PhenDNRT)* uses a binary black hole (BBH) baseline given by the phenomenological frequency-domain model IMRPhenomD, which was introduced in Refs. [79, 80] and calibrated to untuned EOB waveforms [81], as well as numerical-relativity hybrids. The model describes spin-aligned systems throughout the inspiral, merger, and ringdown. The BBH model is augmented by the NRTidal phase description of Refs. [82, 83], which is based on analytical PN knowledge up to 6PN order, a tidal EOB model [84, 85], and numerical-relativity simulations. In PhenDNRT, no additional contributions from EOS-dependent spin-spin or cubic-in-spin effects are included.

*IMRPhenomD-NRTidalv2 (PhenDNRTv2)* uses the same underlying BBH model as PhenDNRT, but has a different description of the tidal sector and the NRTidalv2 phase contribution is employed [59]. This tidal description incorporates PN information up to 7.5PN order and is calibrated to an updated set of tidal EOB and NR waveforms as outlined in Ref. [59]. These updates also include tidal contributions to the GW amplitude as well as the EOS-dependence on the quadrupole and octupole moment in the spin-spin (up to 3PN order) and cubic-in spin (up to 3.5PN order) contributions.

*SEOBNRv4-ROM-NRTidalv2 (SEOBNRTv2)* also uses the NRTidalv2 description for the tidal sector which includes amplitude- and EOS-dependent spin effects. However, in contrast to PhenDNRTv2, the waveform model is based on an effective-one body description. The underlying BBH waveform model SEOBNRv4 was introduced in Ref. [86] and its reduced-order model SEOBNRv4-ROM is constructed following the methods outlined in Ref. [87]. The differences between PhenDNRTv2 and SEOBNRTv2 will enable us to understand the importance of the underlying BBH model for the inference of the EOS parameters.

The variety of employed waveform models allows us to

<sup>2</sup> We note that we employ the existing publicly available TF2 implementation in LALSuite that was used for the analysis of previous GW detections but does not incorporate recently updated 7PN and 7.5PN order terms [77, 78].

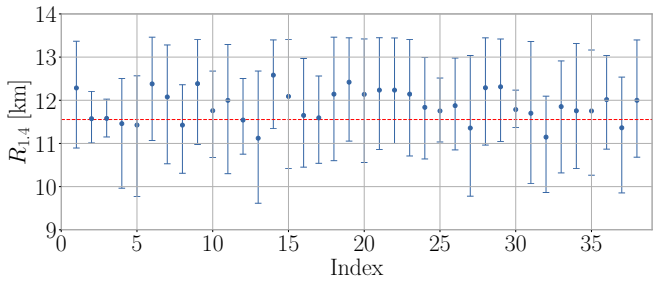


FIG. 2. Constraints on the radius of a typical NS  $R_{1.4}$  from simulated raw data for the injection model PhenDNRTv2. The radius for the injected EOS is shown as red dashed line.

disentangle the effects of the tidal contribution, comparing PhenDNRT vs. PhenDNRTv2, and the point-particle information, comparing PhenDNRTv2 vs. SEOBNRTv2. The comparison against TF2 serves as a “worst case” scenario in which both point-particle and tidal contributions are varied with respect to the injected waveform set.

While the interpretation of the point-particle differences among the waveform models is difficult, an easy interpretation of the tidal contribution for our employed models can be extracted from Fig. 1, where the 7.5PN order (as employed in TF2 in this work), the NRTidal, and the NRTidalv2 frequency-domain phase contribution are shown. NRTidalv2 clearly predicts larger tidal effects than the 7.5PN order contribution and smaller tidal effects than NRTidal for the same tidal deformability. Hence, it is expected that NRTidal models will predict smaller NS radii and TaylorF2 will potentially predict larger radii with respect to our reference model NRTidalv2.

Considering the differences in the employed point-particle contribution, we refer to Fig. 3 of Ref. [36], where it was found that when using the same tidal contribution both TaylorF2 and SEOBNRv4\_ROM lead to smaller estimated tidal deformabilities than IMRPhenomD. A summary of the expected biases and the final result is given in Tab. I.

#### D. Injection setup

A network of interferometers consisting of Advanced LIGO and Advanced Virgo at design sensitivity is simulated [46, 47]. The BNS sources in our injection set are uniformly distributed in a co-moving volume with the optimal network SNR  $\rho$  ranging within  $\rho \in [7, 100]$ . The sources’ sky locations  $(\alpha, \delta)$  and the orientations  $(\iota, \psi)$  are placed uniformly on a sphere. Based on the observed BNS population the spins of NSs are expected to be small [88], and we have restricted the spin magnitudes of the two stars  $(a_1, a_2)$  to be uniformly distributed,  $a_i \in [-0.05, 0.05]$ . The component masses are sampled from a uniform distribution of  $m_{1,2} \in [1, 2] M_\odot$ . For our 40 BNS setups, we have used PhenDNRTv2 as injection

model which led to a total of 160 injections and from the most-likely EOS of Ref. [13], employed in this study, we find that the injected radius of a typical  $1.4M_\odot$  NS,  $R_{1.4}$ , to be  $\sim 11.55$ km corresponding to a dimensionless tidal deformability of  $\Lambda_{1.4} \sim 292.46$ . A first analysis of our obtained injection data revealed that two injections did not converge in the sampling process for all waveform models. Hence, our NS radius measurement results, described in the following, are based on 38 configurations.

### III. RESULTS

#### A. Radius measurements and intrinsic biases

Based on the injection setup described before, we extract the tidal deformabilities of the individual events. In Fig. 2, we present our results for the NS radius,  $R_{1.4}$ , for the injection model PhenDNRTv2. In this figure, we show our simulated population ordered by the injection number, i.e., a random identifier used during the study. The results for  $R_{1.4}$  represent preliminary estimates obtained from our raw data for each individual injected GW event, whereas the uncertainties reflect the 90% confidence intervals. Depending on the source properties, the SNR and the particular noise realisation, different GW events place tighter or weaker constraints on the neutron star radius.

To improve our radius estimate and constraints on the underlying EOSs, one can combine multiple GW events. In Fig. 3, we show the  $R_{1.4}$  results for successively combined GW events. Fig. 3(a) clearly shows that the combination of multiple GW events significantly reduces the uncertainty of a NS radius measurement. Furthermore, in order to avoid an arbitrary ordering effect, we randomly reshuffle the order of the 40 simulated events for 1000 times and compute the median over all permutations; cf. Fig. 3(b).

At this stage, our study still includes an additional selection bias of the tested gravitational-wave population due to our inability of detecting arbitrarily weak GW signals [57]. Therefore, we are systematically more sensitive to sources with higher SNRs. In our case, this means that more massive binaries are favoured due to their high SNRs. Because these systems also correspond to lower tidal deformabilities, this selection effect could lead to smaller  $R_{1.4}$ -predictions. When correcting for this selection bias using the neural network classifier of Ref. [58], we obtain our final result for  $R_{1.4}$  shown in Fig. 3(c). We recover the expected  $\sim 1/\sqrt{N}$  falloff of the statistical uncertainty of the radius measurement, where  $N$  denotes the number of combined GW detections. When all GW events are combined, we obtain a final NS radius estimate for the injection model PhenDNRTv2 of  $11.55^{+0.24}_{-0.25}$ km which is in perfect agreement with the injected value for the NS radius of 11.55km (red dashed line). The injection set corrections illustrated in the different panels of Fig. 3 were likewise applied to the other

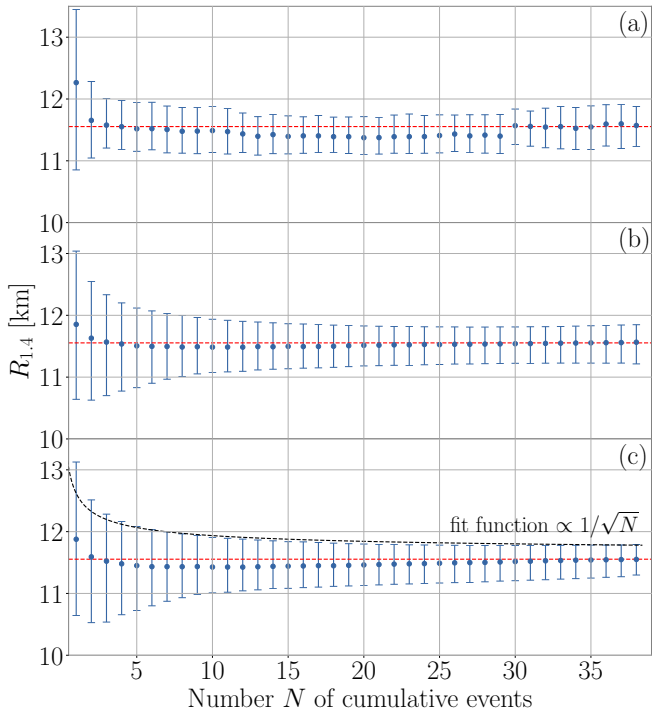


FIG. 3. Overview of the applied injection set corrections for the injection model PhenDNRTv2: (a) combined injection data, (b) combined and randomly reshuffled injection data, and (c) same data as before but corrected for the selection effect as detailed in Sec. II. The injected NS radius is 11.55 km and is shown as red-dashed line.

waveform models used in this study. The final NS radius measurements for all waveform models are listed in Tab. I and are shown in Fig. 4.

From our NS radius measurement for the injection model PhenDNRTv2, we conclude that our results are in agreement with the findings of Ref. [40] who found that the tidal deformability can be measured with a statistical uncertainty of  $\sim 10\%$  after a few tens of detections.

## B. Waveform-model systematics

In Tab. I, we show our expectations of potential systematic biases originating from different modelling assumptions, which we compare with our final results for all waveform models in Fig. 4. As mentioned before, the injection model PhenDNRTv2 perfectly recovers the injected value, but all other models employed in this study introduce a considerable bias in the NS radius measurement. PhenDNRT predicts lower NS radii which can be explained by the different tidal descriptions in the model PhenDNRT (i.e., NRT) and the injection model (NRTv2). This leads to overall smaller tidal deformabilities, and, hence, to smaller NS radii; cf. Tab. I. Due to this systematic bias and decreasing statistical uncertainties, the model recovers the injected value within the

TABLE I. Overview of the expected and measured shift in the NS radius measurement,  $R_{1.4}$ , for our selected set GW models with respect to PhenDNRTv2.  $\circ$  marks no expected bias,  $\uparrow$  an expected larger radius estimate, and  $\downarrow$  an expected smaller estimated radius, and  $\updownarrow$  notes situations in which competing effects are present. The injected NS radius is 11.55 km. The last two columns list the final result of NS radius measurement and the systematic shift  $\Delta R_{1.4}$  of the median value for each model from the injected value.

Model	$\psi_{\text{pp}}$	$\psi_{\text{T}}$	$\psi$	$R_{1.4}$ [km]	$\Delta R_{1.4}$ [m]
PhenDNRTv2	$\circ$	$\circ$	$\circ$	$11.55^{+0.24}_{-0.25}$	-3
PhenDNRT	$\circ$	$\downarrow$	$\downarrow$	$11.22^{+0.26}_{-0.30}$	-329
SEOBNRTv2	$\downarrow$	$\circ$	$\downarrow$	$11.12^{+0.28}_{-0.25}$	-437
TF2	$\downarrow$	$\uparrow$	$\updownarrow$	$11.71^{+0.24}_{-0.26}$	+158

90% credible interval only when less than 20 GW events are combined. Combining all 38 GW events, PhenDNRT recovers a NS radius of  $11.22^{+0.26}_{-0.30}$  km which is lower than the injected value by  $\sim 300$  m. We note that the bell-shaped PDF curve seen for PhenDNRT in Fig. 4 is an effect of our correction for selection bias as described in Sec. II and is not present when excluding this correction.

We find the same trend towards smaller NS radii for SEOBNRTv2. Here, the different point-particle phase description in the model predicts smaller tidal deformabilities and, hence, smaller NS radii. From the results in Fig. 4, we find that the model is able to recover the injected NS radius in the 90% credible interval when less than 30 GW events are combined. The SEOBNRTv2 model predicts a final NS radius of  $11.12^{+0.28}_{-0.25}$  km when all injections are combined and shows a systematic shift of  $\sim 400$  m towards smaller NS radii. In comparison to the injection model PhenDNRTv2, the systematic biases present in PhenDNRT and SEOBNRTv2 lead to overall smaller NS radii for all combined GW events. However, our analysis of the injection raw data showed that for some individual simulations PhenDNRT predicts slightly larger NS radii than PhenDNRTv2.

Finally, the PN model TF2 shows an indefinite trend for  $R_{1.4}$ , giving smaller NS radii for a smaller number of combined GW events, whereas with more than 23 combined GW events TF2 overestimates the injected NS radius. Notably, this model shows the largest uncertainties when less than 10 GW events are combined. Using all 38 detections, TF2 predicts a NS radius of  $11.71^{+0.24}_{-0.26}$  km which is larger than the injected value by  $\sim 150$  m. The trend of the TF2 model could be explained by the different point-particle and tidal-phase descriptions compared to the injection model PhenDNRTv2. Because the point-particle sector is described up to 3.5PN order whereas tidal effects are included up to 7.5 PN order in TF2, the uncertainties of  $\psi_{\text{pp}}$  will dominate for smaller numbers of combined GW events and lead to smaller NS radii while uncertainties of  $\psi_{\text{T}}$  at 7.5PN order begin to dominate when larger numbers of GW events are combined leading to larger NS radii.

Notably, the  $R_{1.4}$ -estimates combining the first few

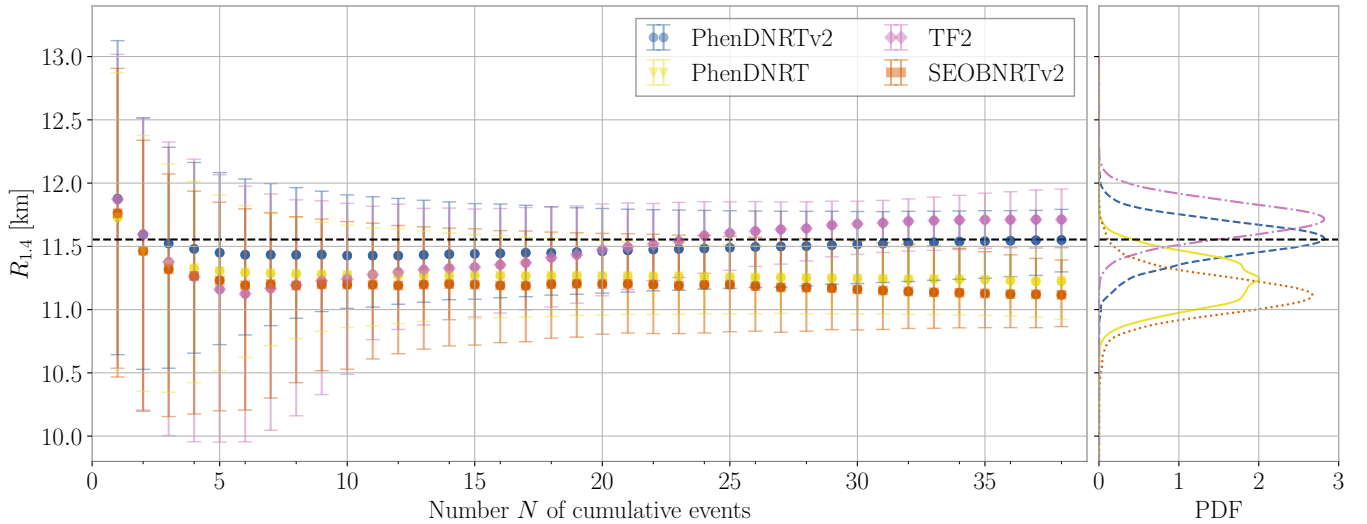


FIG. 4. Constraints on the radius of a typical NS with  $1.4M_{\odot}$ ,  $R_{1.4}$ , versus number of successively combined GW signals for the GW models PhenDNRT, TF2, and SEOBNRTv2 and the injection waveform model PhenDNRTv2. The value for the injected EOS is shown as black-dashed line. The right panel shows the posterior distribution function (PDF) for each waveform model when all simulated GW signals are combined.

events in Fig. 4 follows the same pattern regardless which waveform model is employed. The first event results in an overestimation of  $R_{1.4}$  because it is largely driven by our heavy-pulsar prior. The non-zero support of  $\Lambda = 0$  for low  $\Lambda$  injections results in an underestimation of  $R_{1.4}$  when including few additional events.

We find that our extracted systematic shifts of the NS radius of up to  $\sim 400\text{m}$  are smaller than the one estimated in the study of Ref. [38]. From their mock analysis of 15 binaries, they found that systematic errors dominate over statistical errors from binaries at  $\text{SNR} \gtrsim 80$  and projected a systematic NS radius shift of  $\Delta R \sim 1\text{km}$  for current advanced detectors at design sensitivity. The difference could originate from the fact that we directly sampled over a restricted EOS set in our parameter estimation runs to obtain combined  $R_{1.4}$  estimates, while Ref. [38] used spectral parametrizations and universal relations for the EOS to translate binary tidal parameters into NS EOS and radius information. Consequently, our parameter estimation accounts for more physical information on the NS radius which affects systematic biases. Moreover, systematics only become important once information across several events are combined. As shown in Appendix A, we do not find significant systematic biases when estimating the mass parameters with different waveform models.

#### IV. CONCLUSION

In this work, we have performed a large injection campaign with a total of 160 BNS parameter estimation simulations to understand how the combination of information from multiple BNS detections will decrease statisti-

cal measurement uncertainties in the NS radius and to quantify the impact of waveform model systematics. For this purpose, we have used four different waveform models with different point-particle and tidal phase descriptions. Based on 152 usable BNS simulations, our main findings are summarized below:

- i) We verified that both the combination of multiple GW sources and GW detections with high SNR will be influenced by the different modelling assumptions of existing GW models.
- ii) From a total number of 38 combined simulations, one could constrain the NS radius with an accuracy of  $\pm 250\text{m}$  for our injection model.
- iii) Our results have shown that systematic effects substantially affect the NS radius measurement. In this work, these are strongest for the models PhenDNRT and SEOBNRTv2 (up to  $\sim 440\text{m}$ ). Hence, these models cannot recover the injected NS radius in their 90% credible interval when more than 20 or 30 GW events are combined, respectively.

Overall, with increasing GW detector sensitivity and the projected BNS merger rate of  $10_{-10}^{+52}$  detections per year estimated by [89] or even 9–88 forecasted by [90] for O4, waveform model systematics will influence extracted NS properties. Moreover, it might be possible that systematic uncertainties in GW modelling could lead to inconsistencies in the measured NS properties between different messengers, in particular, when information from electromagnetic counterparts of potential multi-messenger observations or tighter constraints by future X-ray observations similar to [26, 28] are included. In fact, given the expectations of 1 – 13 well-localized

( $\leq 100 \text{ deg}^2$  at 90% credible areas) GW detections for BNS systems with corresponding kilonova detection rates of 0.5–4.8 events per year in O4 [90], one can expect systematic effects when using currently available waveform models in the next observing runs.<sup>3</sup>

## ACKNOWLEDGMENTS

We thank Tatsuya Narikawa and the LVK Extreme Matter group for fruitful discussions and comments on the study. PTHP is supported by the research programme of the Netherlands Organisation for Scientific Research (NWO). The work of I.T. was supported by the U.S. Department of Energy, Office of Science, Office of Nuclear Physics, under contract No. DE-AC52-06NA25396, by the Laboratory Directed Research and Development program of Los Alamos National Laboratory under project numbers 20190617PRD1 and 20190021DR, and by the U.S. Department of Energy, Office of Science, Office of Advanced Scientific Computing Research, Scientific Discovery through Advanced Computing (SciDAC) NUCLEI program. Computational resources have been provided by the Los Alamos National Laboratory Institutional Computing Program, which is supported by the U.S. Department of Energy National Nuclear Security Administration under Contract No. 89233218CNA000001, and by the National Energy Research Scientific Computing Center (NERSC), which is supported by the U.S. Department of Energy, Office of Science, under contract No. DE-AC02-05CH11231. We also acknowledge usage of computer time on Lise/Emmy of the North German Supercomputing Alliance (HLRN) [project bbp00049], on HAWK at the High-Performance Computing Center Stuttgart (HLRS) [project GWanalysis 44189], and on SuperMUC NG of the Leibniz Supercomputing Centre (LRZ) [project pn29ba].

## Appendix A: Assessment on systematic biases on mass parameters

In order to investigate potential biases in the recovery of sources’ mass parameters, i.e., the chirp mass  $\mathcal{M}_c$  and the mass ratio  $q$ , we used a percentile-percentile (pp) test. We expect our recovery to be unbiased when the pp-curve for each parameter follows the  $x = y$  line, apart statistical fluctuations resulting from the Gaussian noise assumed in our BNS simulations.

We find that associated parameters analyzed in Fig. 5 follow the expected  $x = y$  relation, shown as black dashed line, and can be recovered within a  $3\text{-}\sigma$  region ( $2\text{-}\sigma$  for PhenomDNRTv2). In order to quantify deviations seen in Fig. 5, we perform a Kolmogorov-Smirnov (KS) test for all models. Our KS results confirm that the deviations for  $\mathcal{M}_c$  and  $q$  are smallest for our injection model ranging up to a KS statistic  $D_n$  of 0.1 and 0.17, respectively.

As PhenomDNRT has the same point-particle description as PhenomDNRTv2, one expect it to have similar degree of performance as PhenomDNRTv2. Indeed, the PhenomDNRT’s KS statistic are close to the one of PhenomDNRTv2. The KS statistic for chirp mass and mass ratio are 0.11 and 0.20, respectively.

Because PhenomD reduces to TF2 at low frequency, the systematics induced by using TF2 should be less than the one by using SEOB. This matches our results with the TF2’s KS statistic for chirp mass and mass ratio being 0.12 and 0.19, respectively. Because the tidal contribution is only included up to 7PN order for PhenomDNRT, while TF2 has included up to 7.5PN order, that could contributed to the marginally stronger systematics for mass ratio in PhenomDNRT.

While the largest deviation from the  $x = y$  relation is present for SEOBNRTv2 ranging up to 0.12 for  $\mathcal{M}_c$  and 0.22 for  $q$ , we conclude that systematics are not pronounced for these source parameters regardless of waveform model in use.

- 
- [1] B. P. Abbott *et al.* (Virgo, LIGO Scientific), GW170817: Observation of Gravitational Waves from a Binary Neutron Star Inspiral, *Phys. Rev. Lett.* **119**, 161101 (2017), [arXiv:1710.05832 \[gr-qc\]](#).
- [2] B. P. Abbott *et al.* (LIGO Scientific, Virgo), Properties of the binary neutron star merger GW170817, *Phys. Rev.* **X9**, 011001 (2019), [arXiv:1805.11579 \[gr-qc\]](#).

- [3] B. P. Abbott *et al.* (Virgo, LIGO Scientific), GW170817: Measurements of neutron star radii and equation of state, *Phys. Rev. Lett.* **121**, 161101 (2018), [arXiv:1805.11581 \[gr-qc\]](#).
- [4] B. P. Abbott *et al.* (LIGO Scientific, Virgo), GWTC-1: A Gravitational-Wave Transient Catalog of Compact Binary Mergers Observed by LIGO and Virgo during the First and Second Observing Runs, *Phys. Rev.* **X9**, 031040 (2019), [arXiv:1811.12907 \[astro-ph.HE\]](#).
- [5] S. De, D. Finstad, J. M. Lattimer, D. A. Brown, E. Berger, and C. M. Biwer, Tidal Deformabilities and Radii of Neutron Stars from the Observation of GW170817, *Phys. Rev. Lett.* **121**, 091102 (2018), [arXiv:1804.08583 \[astro-ph.HE\]](#).
- [6] A. Bauswein, O. Just, H.-T. Janka, and N. Stergioulas, Neutron-star radius constraints from GW170817 and future detections, *Astrophys. J.* **850**, L34 (2017), [arXiv:1710.06843 \[astro-ph.HE\]](#).

---

<sup>3</sup> Contrasting our statistical uncertainties of 250m after 38 combined detections to the study of [39] which found that a radius statistical uncertainty of 50 – 200m could be present with one GW170817-like event observed either with 3G detectors [91–94] or with a 4-year Voyager operation [95], we conclude that waveform systematics could already become important during the next observing runs, O4 and O5, of Advanced LIGO [46], Advanced VIRGO [47] and KAGRA [96].

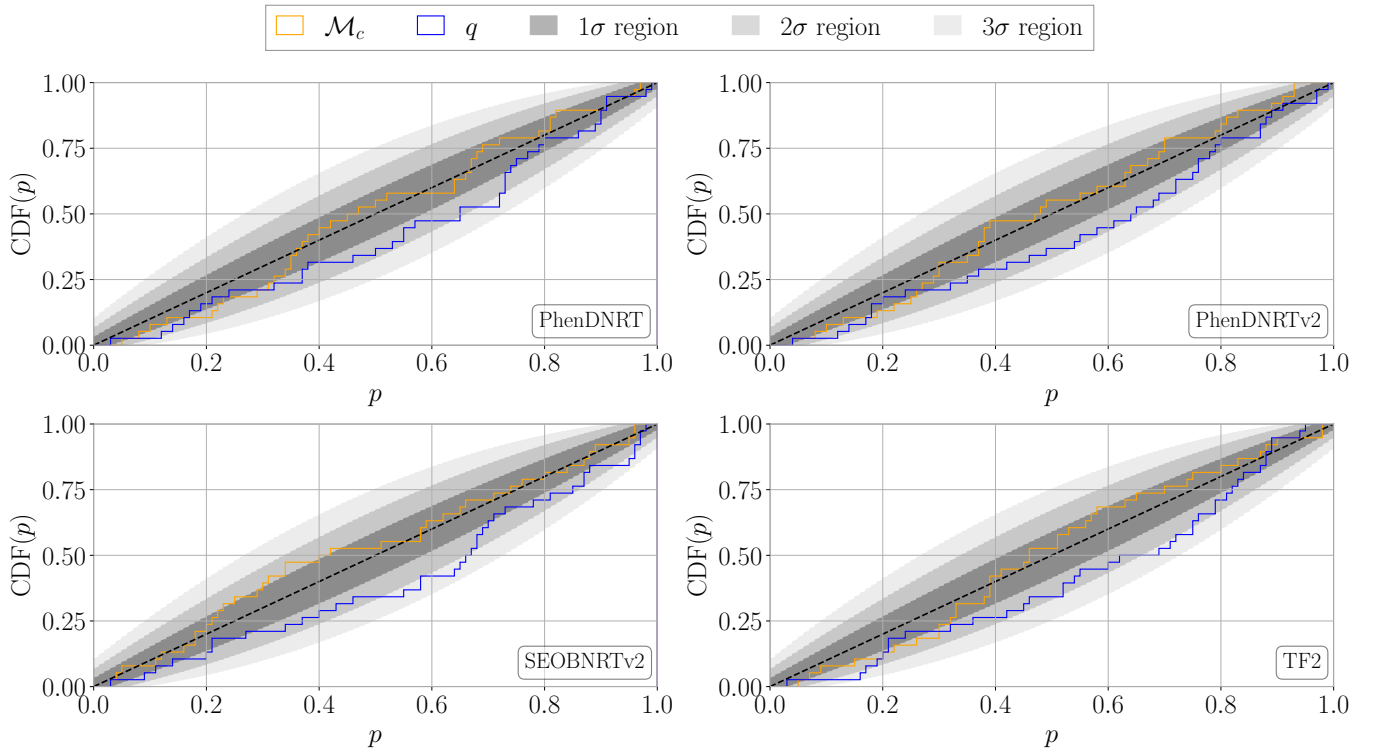


FIG. 5. Percentile-percentile plot for chirp mass  $\mathcal{M}_c$  and mass ratio  $q$  for all waveform models.  $p$  is the probability contained in a given credible interval and  $\text{CDF}(p)$  is the fraction of the injections with their injected values laying inside that interval. The black dashed lines indicates the ideal 1-to-1 relation for the recovery of unbiased parameters. Shaded regions refer to 1-, 2-, and 3- $\sigma$  regions.

- [7] E. Annala, T. Gorda, A. Kurkela, and A. Vuorinen, Gravitational-wave constraints on the neutron-star-matter Equation of State, *Phys. Rev. Lett.* **120**, 172703 (2018), [arXiv:1711.02644 \[astro-ph.HE\]](#).
- [8] E. R. Most, L. R. Weih, L. Rezzolla, and J. Schaffner-Bielich, New constraints on radii and tidal deformabilities of neutron stars from GW170817, *Phys. Rev. Lett.* **120**, 261103 (2018), [arXiv:1803.00549 \[gr-qc\]](#).
- [9] D. Radice and L. Dai, Multimessenger Parameter Estimation of GW170817, *Eur. Phys. J. A* **55**, 50 (2019), [arXiv:1810.12917 \[astro-ph.HE\]](#).
- [10] L. Dai, T. Venumadhav, and B. Zackay, Parameter Estimation for GW170817 using Relative Binning, [arXiv:1806.08793](#) (2018).
- [11] T. Hinderer *et al.*, Distinguishing the nature of comparable-mass neutron star binary systems with multimessenger observations: GW170817 case study, *Phys. Rev. D* **100**, 06321 (2019), [arXiv:1808.03836 \[astro-ph.HE\]](#).
- [12] C. D. Capano, I. Tews, S. M. Brown, B. Margalit, S. De, S. Kumar, D. A. Brown, B. Krishnan, and S. Reddy, Stringent constraints on neutron-star radii from multimessenger observations and nuclear theory, *Nature Astronomy* **4**, 625 (2020), [arXiv:1908.10352 \[astro-ph.HE\]](#).
- [13] T. Dietrich, M. W. Coughlin, P. T. H. Pang, M. Bulla, J. Heinzel, L. Issa, I. Tews, and S. Antier, Multimessenger constraints on the neutron-star equation of state and the Hubble constant, *Science* **370**, 1450 (2020), [arXiv:2002.11355 \[astro-ph.HE\]](#).
- [14] I. Legred, K. Chatzioannou, R. Essick, S. Han, and P. Landry, Impact of the PSR J0740+6620 radius constraint on the properties of high-density matter, [arXiv:2106.05313](#) (2021).
- [15] G. Raaijmakers, S. K. Greif, K. Hebeler, T. Hinderer, S. Nissanke, A. Schwenk, T. E. Riley, A. L. Watts, J. M. Lattimer, and W. C. G. Ho, Constraints on the dense matter equation of state and neutron star properties from NICER’s mass-radius estimate of PSR J0740+6620 and multimessenger observations, [arXiv:2105.06981](#) (2021).
- [16] S. Huth *et al.*, Constraining Neutron-Star Matter with Microscopic and Macroscopic Collisions, [arXiv:2107.06229](#) (2021).
- [17] B. P. Abbott *et al.* (Virgo, Fermi-GBM, INTEGRAL, LIGO Scientific), Gravitational Waves and Gamma-Rays from a Binary Neutron Star Merger: GW170817 and GRB 170817A, *Astrophys. J.* **848**, L13 (2017), [arXiv:1710.05834 \[astro-ph.HE\]](#).
- [18] K. Hebeler, J. M. Lattimer, C. J. Pethick, and A. Schwenk, Equation of state and neutron star properties constrained by nuclear physics and observation, *Astrophys. J.* **773**, 11 (2013), [arXiv:1303.4662 \[astro-ph.SR\]](#).
- [19] I. Tews, J. Carlson, S. Gandolfi, and S. Reddy, Constraining the speed of sound inside neutron stars with chiral effective field theory interactions and observations, *Astrophys. J.* **860**, 149 (2018), [arXiv:1801.01923 \[nucl-th\]](#).
- [20] P. Danielewicz, R. Lacey, and W. G. Lynch, Determination of the equation of state of dense matter, *Science*

- 298**, 1592 (2002), [arXiv:nucl-th/0208016](#).
- [21] P. Russotto *et al.*, Results of the ASY-EOS experiment at GSI: The symmetry energy at suprasaturation density, *Phys. Rev. C* **94**, 034608 (2016), [arXiv:1608.04332 \[nucl-ex\]](#).
- [22] D. Adhikari, H. Albataineh, D. Androic, K. Aniol, D. S. Armstrong, T. Averett, C. Ayerbe Gayoso, S. Barcus, V. Bellini, R. S. Beminiwattha, *et al.* (PREX), Accurate Determination of the Neutron Skin Thickness of  $^{208}\text{Pb}$  through Parity-Violation in Electron Scattering, *Phys. Rev. Lett.* **126**, 172502 (2021), [arXiv:2102.10767 \[nucl-ex\]](#).
- [23] J. Antoniadis, P. C. Freire, N. Wex, T. M. Tauris, R. S. Lynch, *et al.*, A Massive Pulsar in a Compact Relativistic Binary, *Science* **340**, 6131 (2013), [arXiv:1304.6875 \[astro-ph.HE\]](#).
- [24] Z. Arzoumanian *et al.* (NANOGrav), The NANOGrav 11-year Data Set: High-precision timing of 45 Millisecond Pulsars, *Astrophys. J. Suppl.* **235**, 37 (2018), [arXiv:1801.01837 \[astro-ph.HE\]](#).
- [25] E. Fonseca *et al.*, Refined Mass and Geometric Measurements of the High-mass PSR J0740+6620, *Astrophys. J. Lett.* **915**, L12 (2021), [arXiv:2104.00880 \[astro-ph.HE\]](#).
- [26] M. C. Miller *et al.*, PSR J0030+0451 Mass and Radius from *NICER* Data and Implications for the Properties of Neutron Star Matter, *Astrophys. J. Lett.* **887**, L24 (2019), [arXiv:1912.05705 \[astro-ph.HE\]](#).
- [27] T. E. Riley *et al.*, A *NICER* View of PSR J0030+0451: Millisecond Pulsar Parameter Estimation, *Astrophys. J. Lett.* **887**, L21 (2019), [arXiv:1912.05702 \[astro-ph.HE\]](#).
- [28] M. C. Miller *et al.*, The Radius of PSR L0740+6620 from *NICER* and XMM-Newton Data, [arXiv:2105.06979 \(2021\)](#).
- [29] T. E. Riley *et al.*, A *NICER* View of the Massive Pulsar PSR J0740+6620 Informed by Radio Timing and XMM-Newton Spectroscopy, [arXiv:2105.06980 \(2021\)](#).
- [30] L. Blanchet, Gravitational Radiation from Post-Newtonian Sources and Inspiralling Compact Binaries, *Living Rev. Relativity* **17**, 2 (2014), [arXiv:1310.1528 \[gr-qc\]](#).
- [31] A. Buonanno and T. Damour, Effective one-body approach to general relativistic two-body dynamics, *Phys. Rev. D* **59**, 084006 (1999), [arXiv:gr-qc/9811091](#).
- [32] A. Buonanno and T. Damour, Transition from inspiral to plunge in binary black hole coalescences, *Phys. Rev. D* **62**, 064015 (2000), [arXiv:gr-qc/0001013](#).
- [33] L. Baiotti and L. Rezzolla, Binary neutron star mergers: a review of Einstein's richest laboratory, *Rept. Prog. Phys.* **80**, 096901 (2017), [arXiv:1607.03540 \[gr-qc\]](#).
- [34] T. Dietrich, T. Hinderer, and A. Samajdar, Interpreting Binary Neutron Star Mergers: Describing the Binary Neutron Star Dynamics, Modelling Gravitational Waveforms, and Analyzing Detections, *Gen. Rel. Grav.* **53**, 27 (2021), [arXiv:2004.02527 \[gr-qc\]](#).
- [35] R. Dudi, F. Pannarale, T. Dietrich, M. Hannam, S. Bernuzzi, F. Ohme, and B. Brügmann, Relevance of tidal effects and post-merger dynamics for binary neutron star parameter estimation, *Phys. Rev. D* **98**, 084061 (2018), [arXiv:1808.09749 \[gr-qc\]](#).
- [36] A. Samajdar and T. Dietrich, Waveform systematics for binary neutron star gravitational wave signals: effects of the point-particle baseline and tidal descriptions, *Phys. Rev. D* **98**, 124030 (2018), [arXiv:1810.03936 \[gr-qc\]](#).
- [37] A. Samajdar and T. Dietrich, Waveform systematics for binary neutron star gravitational wave signals: Effects of spin, precession, and the observation of electromagnetic counterparts, *Phys. Rev. D* **100**, 024046 (2019), [arXiv:1905.03118 \[gr-qc\]](#).
- [38] R. Gamba, M. Breschi, S. Bernuzzi, M. Agathos, and A. Nagar, Waveform systematics in the gravitational-wave inference of tidal parameters and equation of state from binary neutron star signals, *Phys. Rev. D* **103**, 124015 (2021), [arXiv:2009.08467 \[gr-qc\]](#).
- [39] K. Chatziioannou, Uncertainty limits on neutron star radius measurements with gravitational waves, [arXiv:2108.12368 \(2021\)](#), [arXiv:2108.12368 \[gr-qc\]](#).
- [40] W. Del Pozzo, T. G. F. Li, M. Agathos, C. Van Den Broeck, and S. Vitale, Demonstrating the feasibility of probing the neutron star equation of state with second-generation gravitational wave detectors, *Phys. Rev. Lett.* **111**, 071101 (2013), [arXiv:1307.8338 \[gr-qc\]](#).
- [41] M. Agathos, J. Meidam, W. Del Pozzo, T. G. F. Li, M. Tompitak, J. Veitch, S. Vitale, and C. V. D. Broeck, Constraining the neutron star equation of state with gravitational wave signals from coalescing binary neutron stars, *Phys. Rev. D* **92**, 023012 (2015), [arXiv:1503.05405 \[gr-qc\]](#).
- [42] B. D. Lackey and L. Wade, Reconstructing the neutron-star equation of state with gravitational-wave detectors from a realistic population of inspiralling binary neutron stars, *Phys. Rev. D* **91**, 043002 (2015), [arXiv:1410.8866 \[gr-qc\]](#).
- [43] D. Wysocki, R. O'Shaughnessy, L. Wade, and J. Lange, Inferring the neutron star equation of state simultaneously with the population of merging neutron stars, [arXiv:2001.01747 \(2020\)](#), [arXiv:2001.01747 \[gr-qc\]](#).
- [44] M. Favata, Systematic parameter errors in inspiraling neutron star binaries, *Phys. Rev. Lett.* **112**, 101101 (2014), [arXiv:1310.8288 \[gr-qc\]](#).
- [45] L. Wade, J. D. E. Creighton, E. Ochsner, B. D. Lackey, B. F. Farr, T. B. Littenberg, and V. Raymond, Systematic and statistical errors in a bayesian approach to the estimation of the neutron-star equation of state using advanced gravitational wave detectors, *Phys. Rev. D* **89**, 103012 (2014), [arXiv:1402.5156 \[gr-qc\]](#).
- [46] J. Aasi *et al.* (LIGO Scientific), Advanced LIGO, *Class. Quant. Grav.* **32**, 074001 (2015), [arXiv:1411.4547 \[gr-qc\]](#).
- [47] F. Acernese *et al.* (VIRGO), Advanced Virgo: a second-generation interferometric gravitational wave detector, *Class. Quant. Grav.* **32**, 024001 (2015), [arXiv:1408.3978 \[gr-qc\]](#).
- [48] J. Veitch *et al.*, Parameter estimation for compact binaries with ground-based gravitational-wave observations using the LALInference software library, *Phys. Rev. D* **91**, 042003 (2015), [arXiv:1409.7215 \[gr-qc\]](#).
- [49] J. Skilling, Nested sampling for general Bayesian computation, *Bayesian Analysis* **1**, 833 (2006).
- [50] R. J. E. Smith, G. Ashton, A. Vajpeyi, and C. Talbot, Massively parallel Bayesian inference for transient gravitational-wave astronomy, *Mon. Not. Roy. Astron. Soc.* **498**, 4492 (2020), [arXiv:1909.11873 \[gr-qc\]](#).
- [51] I. Tews, J. Margueron, and S. Reddy, Critical examination of constraints on the equation of state of dense matter obtained from GW170817, *Phys. Rev. C* **98**, 045804 (2018), [arXiv:1804.02783 \[nucl-th\]](#).
- [52] E. Epelbaum, H.-W. Hammer, and U.-G. Meissner, Modern Theory of Nuclear Forces, *Rev. Mod. Phys.* **81**, 1773 (2009), [arXiv:0811.1338 \[nucl-th\]](#).

- [53] R. Machleidt and D. R. Entem, Chiral effective field theory and nuclear forces, *Phys. Rept.* **503**, 1 (2011), [arXiv:1105.2919 \[nucl-th\]](#).
- [54] Z. Arzoumanian *et al.* (NANOGrav), The NANOGrav 11-year Data Set: High-precision timing of 45 Millisecond Pulsars, *Astrophys. J. Suppl.* **235**, 37 (2018), [arXiv:1801.01837 \[astro-ph.HE\]](#).
- [55] E. Fonseca *et al.*, Refined Mass and Geometric Measurements of the High-mass PSR J0740+6620, *Astrophys. J. Lett.* **915**, L12 (2021), [arXiv:2104.00880 \[astro-ph.HE\]](#).
- [56] L. Rezzolla, E. R. Most, and L. R. Weih, Using gravitational-wave observations and quasi-universal relations to constrain the maximum mass of neutron stars, *Astrophys. J.* **852**, L25 (2018), [arXiv:1711.00314 \[astro-ph.HE\]](#).
- [57] I. Mandel, W. M. Farr, and J. R. Gair, Extracting distribution parameters from multiple uncertain observations with selection biases, *Mon. Not. Roy. Astron. Soc.* **486**, 1086 (2019), [arXiv:1809.02063 \[physics.data-an\]](#).
- [58] D. Gerosa, G. Pratten, and A. Vecchio, Gravitational-wave selection effects using neural-network classifiers, *Phys. Rev. D* **102**, 103020 (2020), [arXiv:2007.06585 \[astro-ph.HE\]](#).
- [59] T. Dietrich, A. Samajdar, S. Khan, N. K. Johnson-McDaniel, R. Dudi, and W. Tichy, Improving the NR-Tidal model for binary neutron star systems, *Phys. Rev. D* **100**, 044003 (2019), [arXiv:1905.06011 \[gr-qc\]](#).
- [60] T. Hinderer, B. D. Lackey, R. N. Lang, and J. S. Read, Tidal deformability of neutron stars with realistic equations of state and their gravitational wave signatures in binary inspiral, *Phys. Rev. D* **81**, 123016 (2010), [arXiv:0911.3535 \[astro-ph.HE\]](#).
- [61] T. Hinderer, Tidal Love numbers of neutron stars, *Astrophys. J.* **677**, 1216 (2008), [arXiv:0711.2420 \[astro-ph\]](#).
- [62] T. Damour and A. Nagar, Relativistic tidal properties of neutron stars, *Phys. Rev. D* **80**, 084035 (2009), [arXiv:0906.0096 \[gr-qc\]](#).
- [63] T. Binnington and E. Poisson, Relativistic theory of tidal Love numbers, *Phys. Rev. D* **80**, 084018 (2009), [arXiv:0906.1366 \[gr-qc\]](#).
- [64] B. S. Sathyaprakash and S. V. Dhurandhar, Choice of filters for the detection of gravitational waves from coalescing binaries, *Phys. Rev. D* **44**, 3819 (1991).
- [65] L. Blanchet, T. Damour, B. R. Iyer, C. M. Will, and A. Wiseman, Gravitational radiation damping of compact binary systems to second post-Newtonian order, *Phys.Rev.Lett.* **74**, 3515 (1995).
- [66] T. Damour, P. Jaranowski, and G. Schafer, Dimensional regularization of the gravitational interaction of point masses, *Phys. Lett. B* **513**, 147 (2001), [arXiv:gr-qc/0105038](#).
- [67] L. Blanchet, T. Damour, G. Esposito-Farese, and B. R. Iyer, Gravitational radiation from inspiralling compact binaries completed at the third post-Newtonian order, *Phys.Rev.Lett.* **93**, 091101 (2004), [arXiv:gr-qc/0406012 \[gr-qc\]](#).
- [68] L. Blanchet, T. Damour, G. Esposito-Farese, and B. R. Iyer, Dimensional regularization of the third post-Newtonian gravitational wave generation from two point masses, *Phys. Rev. D* **71**, 124004 (2005), [arXiv:gr-qc/0503044](#).
- [69] C. K. Mishra, A. Kela, K. G. Arun, and G. Faye, Ready-to-use post-Newtonian gravitational waveforms for binary black holes with nonprecessing spins: An update, *Phys. Rev. D* **93**, 084054 (2016), [arXiv:1601.05588 \[gr-qc\]](#).
- [70] B. Mikoczi, M. Vasuth, and L. A. Gergely, Self-interaction spin effects in inspiralling compact binaries, *Phys. Rev. D* **71**, 124043 (2005), [arXiv:astro-ph/0504538](#).
- [71] K. G. Arun, A. Buonanno, G. Faye, and E. Ochsner, Higher-order spin effects in the amplitude and phase of gravitational waveforms emitted by inspiraling compact binaries: Ready-to-use gravitational waveforms, *Phys. Rev. D* **79**, 104023 (2009), [Erratum: *Phys. Rev. D* **84**, 049901 (2011)], [arXiv:0810.5336 \[gr-qc\]](#).
- [72] A. Bohé, G. Faye, S. Marsat, and E. K. Porter, Quadratic-in-spin effects in the orbital dynamics and gravitational-wave energy flux of compact binaries at the 3PN order, *Class. Quant. Grav.* **32**, 195010 (2015), [arXiv:1501.01529 \[gr-qc\]](#).
- [73] T. Damour and A. Nagar, Effective One Body description of tidal effects in inspiralling compact binaries, *Phys. Rev. D* **81**, 084016 (2010), [arXiv:0911.5041 \[gr-qc\]](#).
- [74] J. Vines, E. E. Flanagan, and T. Hinderer, Post-1-Newtonian tidal effects in the gravitational waveform from binary inspirals, *Phys. Rev. D* **83**, 084051 (2011), [arXiv:1101.1673 \[gr-qc\]](#).
- [75] D. Bini, T. Damour, and G. Faye, Effective action approach to higher-order relativistic tidal interactions in binary systems and their effective one body description, *Phys.Rev. D* **85**, 124034 (2012), [arXiv:1202.3565 \[gr-qc\]](#).
- [76] T. Damour, A. Nagar, and L. Villain, Measurability of the tidal polarizability of neutron stars in late-inspiral gravitational-wave signals, *Phys.Rev. D* **85**, 123007 (2012), [arXiv:1203.4352 \[gr-qc\]](#).
- [77] Q. Henry, G. Faye, and L. Blanchet, Tidal effects in the gravitational-wave phase evolution of compact binary systems to next-to-next-to-leading post-Newtonian order, *Phys. Rev. D* **102**, 044033 (2020), [arXiv:2005.13367 \[gr-qc\]](#).
- [78] T. Narikawa, N. Uchikata, and T. Tanaka, Gravitational-wave constraints on the GWTC-2 events by measuring the tidal deformability and the spin-induced quadrupole moment (2021), [arXiv:2106.09193 \[gr-qc\]](#).
- [79] S. Husa, S. Khan, M. Hannam, M. Pürrer, F. Ohme, X. Jiménez Forteza, and A. Bohé, Frequency-domain gravitational waves from nonprecessing black-hole binaries. I. New numerical waveforms and anatomy of the signal, *Phys. Rev. D* **93**, 044006 (2016), [arXiv:1508.07250 \[gr-qc\]](#).
- [80] S. Khan, S. Husa, M. Hannam, F. Ohme, M. Pürrer, X. Jiménez Forteza, and A. Bohé, Frequency-domain gravitational waves from nonprecessing black-hole binaries. II. A phenomenological model for the advanced detector era, *Phys. Rev. D* **93**, 044007 (2016), [arXiv:1508.07253 \[gr-qc\]](#).
- [81] A. Taracchini, A. Buonanno, Y. Pan, T. Hinderer, M. Boyle, *et al.*, Effective-one-body model for black-hole binaries with generic mass ratios and spins, *Phys.Rev. D* **89**, 061502 (2014), [arXiv:1311.2544 \[gr-qc\]](#).
- [82] T. Dietrich, S. Bernuzzi, and W. Tichy, Closed-form tidal approximants for binary neutron star gravitational waveforms constructed from high-resolution numerical relativity simulations, *Phys. Rev. D* **96**, 121501 (2017), [arXiv:1706.02969 \[gr-qc\]](#).
- [83] T. Dietrich *et al.*, Matter imprints in waveform models for neutron star binaries: Tidal and self-spin effects, *Phys. Rev. D* **99**, 024029 (2019), [arXiv:1804.02235 \[gr-qc\]](#).

- [84] A. Nagar *et al.*, Time-domain effective-one-body gravitational waveforms for coalescing compact binaries with nonprecessing spins, tides and self-spin effects, *Phys. Rev. D* **98**, 104052 (2018), [arXiv:1806.01772 \[gr-qc\]](#).
- [85] S. Bernuzzi, A. Nagar, T. Dietrich, and T. Damour, Modeling the Dynamics of Tidally Interacting Binary Neutron Stars up to the Merger, *Phys.Rev.Lett.* **114**, 161103 (2015), [arXiv:1412.4553 \[gr-qc\]](#).
- [86] A. Bohé *et al.*, Improved effective-one-body model of spinning, nonprecessing binary black holes for the era of gravitational-wave astrophysics with advanced detectors, *Phys. Rev. D* **95**, 044028 (2017), [arXiv:1611.03703 \[gr-qc\]](#).
- [87] M. Pürrer, Frequency domain reduced order models for gravitational waves from aligned-spin compact binaries, *Class. Quant. Grav.* **31**, 195010 (2014), [arXiv:1402.4146 \[gr-qc\]](#).
- [88] R. W. O’Shaughnessy, C. Kim, V. Kalogera, and K. Belczynski, Constraining population synthesis models via empirical binary compact object merger and supernovae rates, *Astrophys. J.* **672**, 479 (2008), [arXiv:astro-ph/0610076](#).
- [89] B. P. Abbott *et al.* (KAGRA, LIGO Scientific, Virgo), Prospects for observing and localizing gravitational-wave transients with Advanced LIGO, Advanced Virgo and KAGRA, *Living Rev. Rel.* **23**, 3 (2020).
- [90] P. Petrov, L. P. Singer, M. W. Coughlin, V. Kumar, M. Almualla, S. Anand, M. Bulla, T. Dietrich, F. Foucart, and N. Guessoum, Data-driven expectations for electromagnetic counterpart searches based on ligo/virgo public alerts (2021), [arXiv:2108.07277 \[astro-ph.HE\]](#).
- [91] B. P. Abbott *et al.* (LIGO Scientific), Exploring the Sensitivity of Next Generation Gravitational Wave Detectors, *Class. Quant. Grav.* **34**, 044001 (2017), [arXiv:1607.08697 \[astro-ph.IM\]](#).
- [92] M. Punturo *et al.*, The third generation of gravitational wave observatories and their science reach, *Class. Quant. Grav.* **27**, 084007 (2010).
- [93] S. Hild *et al.*, Sensitivity Studies for Third-Generation Gravitational Wave Observatories, *Class. Quant. Grav.* **28**, 094013 (2011), [arXiv:1012.0908 \[gr-qc\]](#).
- [94] D. Reitze *et al.*, Cosmic Explorer: The U.S. Contribution to Gravitational-Wave Astronomy beyond LIGO, *Bull. Am. Astron. Soc.* **51**, 035 (2019), [arXiv:1907.04833 \[astro-ph.IM\]](#).
- [95] R. X. Adhikari *et al.* (LIGO), A cryogenic silicon interferometer for gravitational-wave detection, *Class. Quant. Grav.* **37**, 165003 (2020), [arXiv:2001.11173 \[astro-ph.IM\]](#).
- [96] T. Akutsu *et al.* (KAGRA), Overview of KAGRA: Detector design and construction history (2020), [arXiv:2005.05574 \[physics.ins-det\]](#).